

Computer-generated hologram cavity interferometry test for large x-ray mirror mandrels: design

Guangjun Gao, MEMBER SPIE
National Institute of Standards and Technology
Manufacturing Engineering Laboratory
100 Bureau Drive
Gaithersburg, Maryland 20899-8223
E-mail: Guangjun.gao@nist.gov

John P. Lehan, MEMBER SPIE
NASA Goddard Space Flight Center
8800 Greenbelt Road
Greenbelt, Maryland 20770
and
University of Maryland
Department of Physics
1000 Hilltop Circle
Baltimore, Maryland 21250

William W. Zhang
NASA Goddard Space Flight Center
8800 Greenbelt Road
Greenbelt, Maryland 20770

Ulf Griesmann
Johannes A. Soons
National Institute of Standards and Technology
Manufacturing Engineering Laboratory
100 Bureau Drive
Gaithersburg, Maryland 20899-8223

1 Introduction

X-ray optical technology finds important roles in astronomy, microscopy, and lithography. For soft x-rays or extreme ultraviolet photons, material absorption precludes transmissive optics. Because the refractive index of all materials is slightly less than unity in the x-ray region, mirrors operate by total external reflection. These two factors combine to make most x-ray imaging systems grazing-incident reflection systems. For broadband performance, the systems tend to have large F-numbers and, in combination with grazing-incidence operation, the optics tend to have large ratios of the radii of curvatures in planes parallel and orthogonal to the system axis. Typical designs employ very far off-axis (near 90 deg) conic sections (hyperboloids, paraboloids, or ellipsoids).¹

Some x-ray mirror systems are nested to achieve high throughput and aperture efficiency. This is particularly true for space-based systems where weight and size considerations are paramount and the source is weak. These mirrors are currently made via replication from mandrels.²⁻⁴ How-

Abstract. A glancing-incidence interferometric test for large x-ray mirror mandrels, using two computer-generated holograms (CGHs), is described. The two CGHs are used to form a double-pass glancing-incidence system. One layout of the CGH-cavity glancing-incidence interferometer is studied and factors relating to its design are analyzed. A semianalytical expression for the phase function is derived that avoids high-order ripple errors and improves the efficiency of the CGH pattern generation. A system of coarse and fine fiducials for establishing the CGH-cavity and aligning the tested mandrel is discussed. Compared with traditional measurement devices, such as coordinate measuring machines (CMMs) or other scanning metrology systems, the CGH-cavity glancing-incidence interferometer can measure a mandrel surface without mechanical contact, at a high spatial sampling frequency, with lower uncertainty, and at high speed. © 2009 Society of Photo-Optical Instrumentation Engineers. [DOI: 10.1117/1.3153303]

Subject terms: computer-generated hologram; mandrel; x-ray optics; optical testing; interferometry.

Paper 080939R received Dec. 1, 2008; revised manuscript received Apr. 6, 2009; accepted for publication Apr. 22, 2009; published online Jun. 10, 2009.

ever, standard tests for conic aspheres do not work on the mandrel masters—the nonfocusing conjugate of the focusing replicated mirrors. In addition, in the nested systems, all the optics must come to a common focal point. This places further demands on testing and fabrication, since surface and geometry tests must be combined to gain the characterization required to assure that all the optics are fabricated to the same plate scale demanded by the confocality of the nested systems.

The coordinate measuring machine (CMM) has been the instrument of choice for mandrel characterization. Fawcett⁵ used a CMM with 100-nm resolution and a long trace profiler (LTP),⁶ a scanning differential slope-measuring instrument, to determine the figure of finished mandrels after polishing. Zhang et al.⁷ employed a noncontact cylindrical-geometry CMM system for the geometric measurement of mandrel surfaces. However, the random and systematic errors of such systems make them undesirable for mandrel characterization, particularly during mandrel polishing. In addition, all the methods mentioned (including CMM) are scanning methods, which result in lower spatial resolution, long acquisition times, and concomitant stability issues.

Interferometry with CGHs, conversely, is a mature tech-

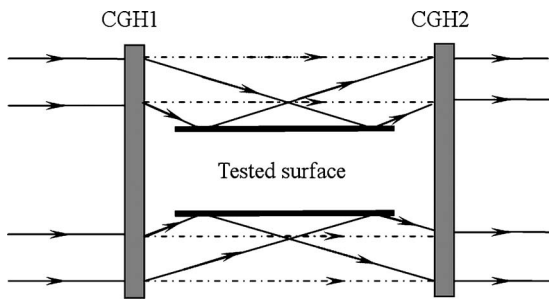


Fig. 1 Glancing-incidence interferometer for testing a cylinder.

nology with excellent spatial resolution. In addition, CGHs can produce very complex wavefronts that are nearly impossible to achieve with traditional optical elements. The adoption of CGH testing of aspheric surfaces has greatly improved the accuracy and efficiency of aspheres, and has broadened the classes of aspheres that designers can employ in practice.

One example, from which we draw our inspiration, is the interferometric form measurement of cylinders proposed by Dresel et al.,⁸ Kulawic,⁹ and Mantel, Lindlein, and Schwider.¹⁰ These authors proposed glancing-incidence interferometers employing two CGHs for testing cylindrical lens surfaces and rod-like object surfaces. Their system is shown schematically in Fig. 1.

A glancing-incidence interferometer can be used to measure the cylindrical surface without the need for a cylindrical reference surface, without contact, and with high spatial fidelity and wavefront accuracy—all important advantages over other testing methods. The concept of a grazing-incidence interferometer, using gratings as a beamsplitter and beam combiner, was originally developed by Birch¹¹ and Hariharan¹² to measure the flatness of ground surfaces. A double-pass version of an oblique-incidence interferometer for flatness metrology, which was later developed by Wilson,¹³ is an approximate analog to the mandrel test we describe in this work.

We extend the ideas of Dresel et al.,⁸ Kulawic,⁹ and Mantel, Lindlein, and Schwider,¹⁰ and apply them to the testing of mandrels for grazing-incidence x-ray mirrors. We call this extension “CGH cavity metrology” and demonstrate by example that it is often possible to use two CGHs to establish a geometry *independent of the optic under test* and thereby conduct both a surface and geometry test simultaneously. Such a test provides the common plate scale needed for multiaperture systems, like x-ray telescopes or the increasingly common segmented primary mirrors of large optical telescopes.

2 Overview of the Problem: Mandrel Metrology

For the International X-ray Observatory (IXO) mission, one of the possible mirror fabrication technologies is replication via glass slumping. The mirrors are slumped over a precisely figured fused silica mandrel. The geometric and figure accuracy of the mandrel needs to be about a factor of 2 better than the desired mirror accuracy to allow for errors in the slumping process. The mission goal for the angular resolution at the time of this writing is 5" half-power diameter (HPD), which is the image space angular subtense where

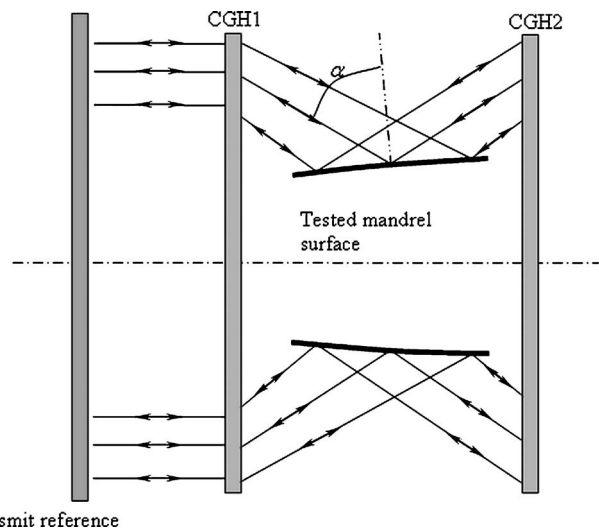


Fig. 2 Conceptual illustration of CGH cavity metrology demonstrating the symmetry breaking of the cavity imposed by the mandrel. Any movement of the mandrel other than rotation about its axis destroys the retrace condition. (Compare with Fig. 1 for the cylinder and its higher symmetry.)

the telescope point spread function falls to 50% of its peak value. This translates to a mirror of around 3" HPD and thus a mandrel of about 1" to 2".

Although modern polishing technology can produce such a nonfocusing optic, the guiding metrology is often inadequate. Modern coordinate measuring equipment seems capable of measuring the geometry of the mandrel, but the sampling is too coarse to yield the surface quality required over the spatial frequency bandwidth required for x-ray optics. Thus, a second metrology method is needed for the surface quality. The registration of the two measurements to the required accuracy is very difficult. Combining the geometric and surface quality measurements into a single test via the CGH cavity metrology method mentioned earlier overcomes the difficulty.

The problem addressed by the test in Fig. 1 is geometrically degenerate. A cylinder can be rotated, translated, and flipped end to end and the wavefront shape is unchanged (see Fig. 1). The mandrels we need to test are paraboloids that are nearly cylinders, breaking most of this geometric degeneracy, having only the rotational symmetry remaining. This proves to be very helpful for mandrel alignment, because the proper wavefront is produced at only one axial position for the mandrel (see Fig. 2).

2.1 Mandrel Metrology Example

To demonstrate the advantages of CGH cavity metrology, we discuss here the case of the design for a specific mandrel for the IXO mission.¹⁴ This is a demonstration project for the mission technology development. The demonstration is a proof of concept and of reduced scale relative to the testing of the flight optics. These differences affect the test accuracy and are mentioned as they arise with the higher-precision flight choice mentioned in passing.

For the mission mandrels, the analog to the Ref. 10 test of Fig 2 would require very large (several hundred millimeter diameter) CGHs for the outer mirror shells. Although

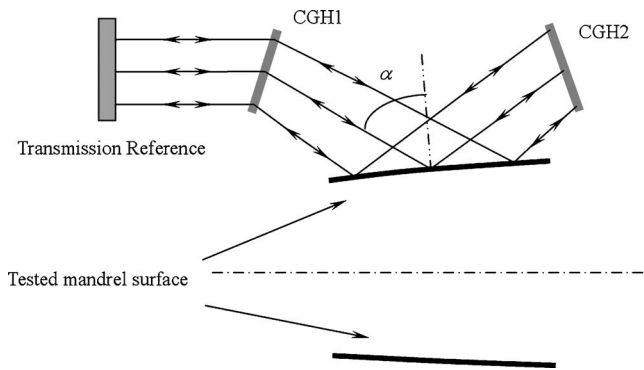


Fig. 3 Schematic layout of the demonstration CGH cavity metrology test for a mandrel. Angles and geometry are exaggerated for clarity. Compare to Figs. 1 and 2.

such CGHs can be made,¹⁵ the substrates are too costly to be practical and also unnecessary for the problem at hand. In the slumping process, only a small fraction of the full 360-deg azimuthal span of the mandrel is used. For IXO's glass mirror technology development, this is 60 deg for the inner mirror shells and 30 deg for the outer mirror shells. Thus, the slumping area need only extend about 10% beyond these boundaries, and the test need only test to these boundaries as well. This results in the CGH substrates for the flight test being sector shaped. To test the entire mandrel, the mandrel can be spindle mounted and rotated and the resulting interferograms stitched. For the demonstration outlined here, we employ round CGH substrates given their reduced cost and greater availability. The round substrates are not fundamental to the methodology, though they compromise the measurement accuracy slightly because of the reduced area testable.

3 First-Order Design Considerations

We began the design with some preliminary geometrical considerations. The first was to develop a test geometry suitable for a Fizeau interferometer. Several configurations were considered, but we settled on a double-pass retrace geometry, as shown in Fig. 3. The system includes an interferometer (only the reference flat is shown), CGH1, CGH2, and the mandrel under test. A collimated beam from the interferometer intersects CGH1, and the resultant diffracted wavefront is incident on the mandrel at angle α . The reflected beam propagates to CGH2, is diffracted (in Littrow) by CGH2, and then propagates along its previous path, arriving back at the interferometer. After the measurement, the mandrel is rotated azimuthally and remeasured. The sequence is repeated until the entire surface has been tested.

We chose this geometry for its greater sensitivity, improved pupil mapping, and best utilization of the interferometer aperture. The improved pupil mapping can be recognized by comparing Figs. 1 and 3. In Fig. 1, when viewed from the interferometer the part under test is only in focus over a limited area. In the reflection geometry (see Fig. 3), however, there is a second image of the mandrel farther from the interferometer that is the "reflection" of the



Fig. 4 Beam footprint on the mandrel under test (units: mm).

mandrel seen through CGH1 and CGH2. This image is approximately in focus over the entire illuminated area of the mandrel.

The next design step is dictated by the interferometer aperture size or CGH size and the mandrel size. In the demonstration, the CGH substrate diameter is about 150 mm, and the mandrel is a paraboloid with a vertex radius of curvature of 0.3906059 mm (design value), a midplane diameter of 250.8 mm, and an axial clear aperture of 275 mm. The CGH1-to-CGH2 cavity center-to-center axial distance was set at 400 mm to allow room for tooling. With a fixed CGH size, to gain sensitivity to mandrel position, we want to illuminate as large an angular and axial span as practical. This implies a larger glancing angle (measured from the surface normal). This, however, reduces the height sensitivity of the test. We settled on an angle of 71.6 deg as a compromise between increased cone angle sensitivity and reduced height sensitivity for a given CGH size. This choice reduces the height sensitivity of the test to 2/3 that of a normal incidence test. The resulting illumination spot on the mandrel is shown in Fig. 4.

The next consideration is throughput of the test. This is a combination of mandrel reflectivity and CGH diffraction efficiency. In our Fizeau interferometer, the reflectivity of the uncoated reference flat is $R_{TR} \approx 4\%$. For the test arm we have,

$$T = (T_{TR})^2 \cdot (D_{CGH1})^2 \cdot (R_{mandrel})^2 \cdot D_{CGH2}, \quad (1)$$

where T_{TR} is the transmittance of the reference flat ($T_{TR} = 96\%$), and D_{CGH1} and D_{CGH2} are the first-order diffraction efficiencies of CGH1 and CGH2, respectively (see Fig. 2). $R_{mandrel}$ is the reflectance of the mandrel under test, and T is the transmittance of the entire test setup.

From Eq. (1), the combination of D_{CGH1} , D_{CGH2} , and $R_{mandrel}$ needs to be high enough to approximately match the intensity of the reference beam for best interference contrast. This means we have to employ phase CGHs, and the tested mandrel should be coated with a temporary reflective film (e.g., by galvanic deposition of a silver coating).¹⁶ On substitution into Eq. (1), we have

$$T \approx (0.96)^2 \cdot (0.35)^2 \cdot (0.99)^2 \times 0.35 = 0.0387 = 3.87\%,$$

which is a good match to the intensity of the reference beam.

We discuss the various aspects of the CGH design next for both CGH1 and CGH2, including the design of the fiducials that establish the cavity geometry.

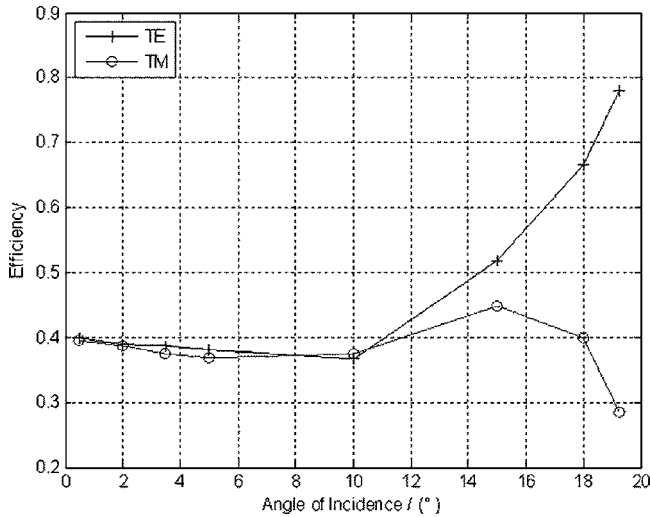


Fig. 5 Efficiency for each polarization component, transverse electric (TE) and transverse magnetic (TM) versus the incidence angle for CGH2 (reflection CGH).

4 Computer-Generated Hologram Design

4.1 Angle of Incidence Effects

Angle of incidence effects fall into three categories: surface height sensitivity, polarization effects, and stray light sensitivity. All these categories should be considered for a high-sensitivity test.

4.1.1 Surface height sensitivity

The angle of incidence on the part affects the height sensitivity as discussed before and is simply scaled by the cosine of the angle of incidence. Thus one wishes to operate as close as practical to normal incidence. Other pragmatic factors, as stated before, prevent us from operating near-normal incidence, so the sensitivity is diminished. The choice of double-pass geometry, however, recovers some of the sensitivity lost from glancing incidence. In our case, the

surface height sensitivity in single pass is one-third that of a normal incidence test, but double pass increases it to two-thirds.

4.1.2 Polarization effects

Because the feature size of the CGHs is comparable with the wavelength, polarization effects cannot be neglected, especially for CGH2, because polarization effects in reflection CGHs are more significant. An appropriate tilt angle of CGH2 should be chosen to assure polarization effects are not significant. Figure 5 plots the efficiency for each polarization versus the incidence angle for CGH2, calculated with the PCGrate-S(X)* program.

From Fig. 5, we can see that the polarization effects are not significant until the angle of incidence for CGH2 exceeds 10 deg from its surface normal. With the increase of the incidence angle beyond 10 deg, the difference between the transverse electric (TE) and transverse magnetic (TM) becomes pronounced. Therefore, we restricted the angle of incidence on CGH2 to less than 10 deg in the design.

4.1.3 Tilt angles of computer-generated holograms and stray light

It is necessary to prevent stray beams from entering the interferometer. The following four cases should be avoided.

1. Tilt angle (relative to the interferometer axis) of CGH1 $\theta_1=0$ deg, as shown in Fig. 6(a). In this case, the reflected rays from the front and rear surface of CGH1 will propagate into the interferometer and result in stray fringes.
2. Tilt angle of CGH2 $\theta_2=(90 \text{ deg}-\alpha)/2$. In this case, part of the zero-order beam of CGH2 can transmit through CGH1 and propagate into the interferometer, as indicated by the dashed line in Fig. 6(b). In addition, the transmitted zero-order beam of CGH1 can be reflected by CGH2 and the tested mandrel, and then diffracted by CGH1 and propagated into the interferometer, which is shown as a double-point dash line in Fig. 6(b).

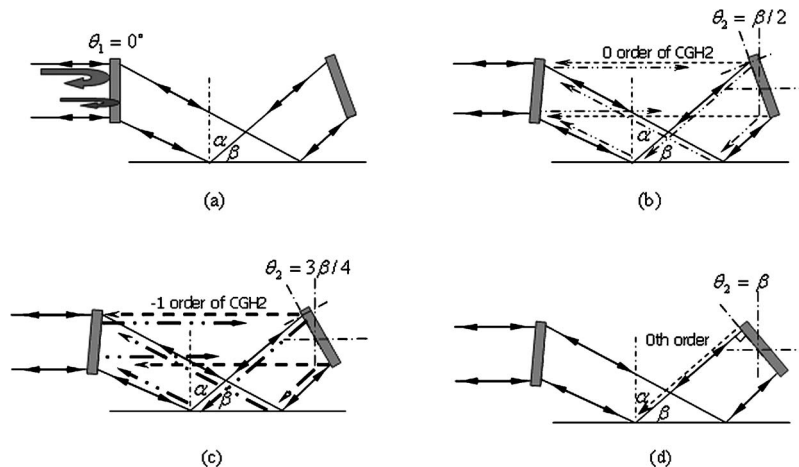


Fig. 6 Four cases where the stray light can result in unwanted interfere fringes for the test setup: (a) $\theta_1=0$ deg, (b) $\theta_2=\beta/2$, (c) $\theta_2=3\beta/4$, and (d) $\theta_2=\beta$, where $\beta=90 \text{ deg}-\alpha$.

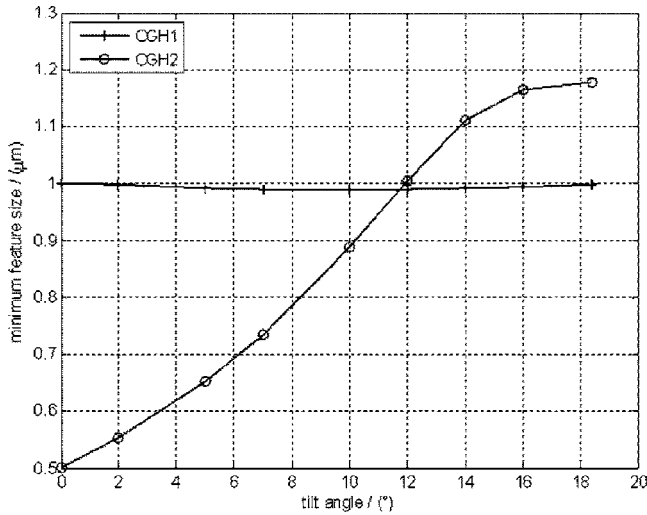


Fig. 7 Relationship between CGH tilt angle (relative to the interferometer axis) and minimum feature size.

3. Tilt angle of CGH2 $\theta_2 = 3(90 \text{ deg} - \alpha) / 4$. This is similar to case 2. A portion of the negative first-order beam of CGH2 can transmit through CGH1 and propagate into the interferometer as indicated by the bold dashed line in Fig. 6(c). Also, the transmitted zero-order beam of CGH1 is diffracted by CGH2 and propagates through mandrel and CGH1 enters into the interferometer, as shown as a bold double-point dash line in Fig. 6(c).
4. Tilt angle of CGH2 $\theta_2 = (90 \text{ deg} - \alpha)$. In this case, the diffracted beam (first order, negative first order) and reflected beam (zero order) cannot be separated enough in the central area of CGH2, so the negative first-order and zero-order diffracted beams will act as strays, as shown by the dashed line in Fig. 6(d).

For cases 2. and 3., part of the stray light can be obscured by placing an opaque screen between CGH1 and CGH2 in the appropriate position. In general, however, it is better to avoid these cases entirely.

4.1.4 Feature size

The tilt angles of the CGHs influence the CGH feature size needed to generate the phase, which are derived explicitly in Sec. 4.2.2. Figure 7 shows this relationship between the minimum feature sizes and tilt angles of CGH1 and CGH2.

CGH1 transmits the incident collimated beam and deviates the beam by 18.4 deg for the geometry chosen earlier. The feature size of CGH1 is quite insensitive to substrate tilt angle. For CGH2, which is used in a Littrow configuration, the feature size becomes smaller when the tilt angle relative to the interferometer decreases, because the diffraction angle increases (see Fig. 3).

We wish to operate with larger feature sizes for two reasons. The first is that, given a constant number of bits for the direct-write lithography process used for CGH fabrication, the relative error decreases. Secondly, for many writing methods, the write time will go down. This usually translates into better accuracy because the thermal drift of the writing platform can be better controlled.

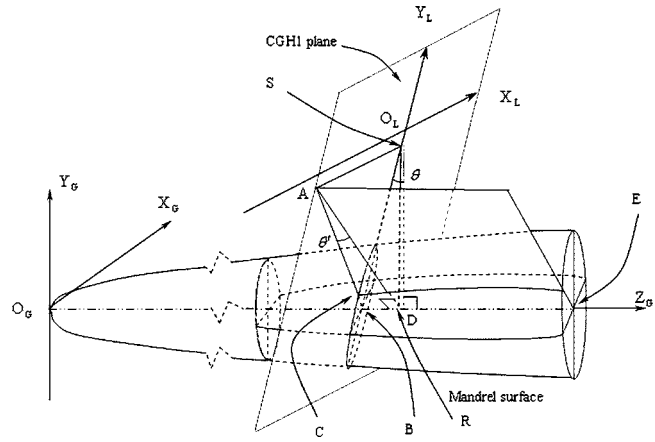


Fig. 8 CGH1 plane and mandrel surface geometry for phase derivation. See text for definitions.

Combining the requirements of feature size, stray light, and polarization effect, the optimum tilt angles of CGH1 and CGH2 can be determined. Given the insensitivity of CGH1 to tilt angle, we set its tilt to 1 deg to avoid stray light case 1. (Sec. 4.1.3). The tilt angle of CGH2 is 10 deg for low polarization and a practical minimum feature size. With these angles, the approximate minimum feature sizes of CGH1 and CGH2 are 1 and 0.88 μm , respectively.

4.2 Main Pattern Design for CGH1 and CGH2

To fabricate CGH1 and CGH2, their phase functions must be known. Generally, Cartesian or radial polynomials are used to express the phase of the CGH in commercial optical design software. The advantage of polynomials is that the phase function is easily determined to the needed overall accuracy from numerical computation. The disadvantage is that there may be ripple (mid-to-high frequency) errors when the order of the polynomial needed for obtaining an adequate fit is high. So finding an analytical or semianalytical expression for the phase functions of CGH1 and CGH2 is desirable. Because the method of derivation is similar for CGH1 and CGH2, we focus in this work on CGH1 and derive a semianalytical expression of its phase function.

4.2.1 Geometry of CGH1 and mandrel surface

The geometry of CGH1 and the mandrel surface is shown in Fig. 8. It shows the spatial relation of the mandrel and CGH1 plane. There are two coordinate systems, the global coordinate system $O_G-X_GY_GZ_G$, with its origin at the vertex of mandrel, and a local coordinate system $O_L-X_LY_LZ_L$, with its origin O_L at the central point of CGH1. The coordinates of O_L in the global system are $(0, y_{CGH}, z_{CGH})$. The plane $X_L O_L Y_L$ is coincident with the CGH1 substrate plane. The relationship between global coordinates and local coordinates is given by the following coordinate transformation,

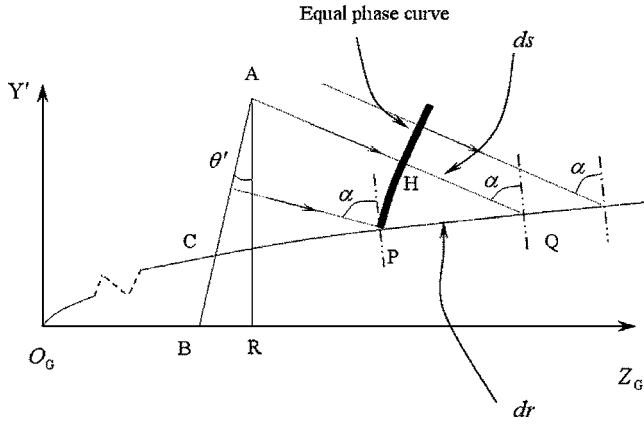


Fig. 9 2-D cross section of CGH1 and the tested mandrel surface.

$$\begin{pmatrix} x_G \\ y_G \\ z_G \end{pmatrix} = \begin{pmatrix} 1 & 0 & 0 \\ 0 & \cos \theta & -\sin \theta \\ 0 & \sin \theta & \cos \theta \end{pmatrix} \begin{pmatrix} x_L \\ y_L \\ z_L \end{pmatrix} + \begin{pmatrix} 0 \\ y_{CGH} \\ z_{CGH} \end{pmatrix}, \quad (2)$$

where θ is the tilt angle of the CGH1 plane relative to the Y_G axis of the global coordinate system. A is a point on the CGH1 plane, with global coordinates (x_G^A, y_G^A, z_G^A) , B is the intersection point of CGH1 plane and Z_G axis, with global coordinates $(0, 0, z_{CGH} - y_{CGH} \tan \theta)$, C is the intersection point of line AB and the mandrel surface, S is the intersection point of the Y_L axis with a plane through point A perpendicular to the Y_L axis, and R is the intersection point of the Z_G axis with a plane through point A perpendicular to the Z_G axis. The angle $\angle RAB$ is designated θ' .

From Fig. 8, we see

$$\tan \theta' = \frac{y_G^A \cdot \tan \theta}{\sqrt{(x_G^A)^2 + (y_G^A)^2}}. \quad (3)$$

4.2.2 Phase function model in a two-dimensional plane

From the schematic layout of Fig. 3, the tested ray (positive first diffraction order) from any point A on the CGH1 surface lies in the plane formed by point A and axis Z_G , as shown in Fig. 8. Actually, the positive first-order rays diffracted from any point on the line AB also lie in this plane. Because the mandrel surface has rotational symmetry about its axis Z_G , we can calculate the phase function in the 2-D plane ABE rather than in the full 3-D space, as illustrated in Fig. 9.

Figure 9 is the 2-D cross section ABE from Fig. 8. Rays diffracted from line AC arrive at the mandrel surface with a glancing angle α . The thick solid curve PH is an equal-phase surface from the CGH.

The tested mandrel surface is a paraboloid, so in Fig. 9 coordinates it takes the form

$$Z = \frac{Y'^2}{2r} \quad (4)$$

where r is the radius of curvature at point O_G , the vertex.

The coordinates of point Q on the mandrel surface $Q(y'^Q, z_G^Q)$ are related to the coordinates of the corresponding point A on the CGH1 surface through the following expression (see the appendix in Sec. 7 for the derivation),

$$\begin{cases} y'^A = \frac{z_{CGH} - y_{CGH} \tan \theta - z_G^Q + Ty'^Q}{T - \tan \theta'} \\ z_G^A = z_{CGH} - y_{CGH} \tan \theta + y'^A \tan \theta' \end{cases}, \quad (5)$$

where

$$T = \frac{-V + \sqrt{V^2 - 4UW}}{2U}, \quad U = \left[\frac{(y'^Q)^2}{r^2} + 1 \right] \cos^2 \alpha - 1,$$

$$V = 2(y'^Q)/r, \quad \text{and } W = U + 1 - \frac{(y'^Q)^2}{r^2}.$$

From Eq. (5), we then have

$$|AQ| = [(y'^A - y'^Q)^2 + (z_G^A - z_G^Q)^2]^{1/2}. \quad (6)$$

Also from Fig. 9, $|HQ| = |PQ| \cdot \sin \alpha$ when distance $|PQ|$ is small enough, we have

$$\begin{aligned} \lim_{|PQ| \rightarrow 0} |HQ| &= ds = dr \cdot \sin \alpha = \sqrt{(dy')^2 + (dz)^2} \cdot \sin \alpha \\ &= \sin \alpha \sqrt{\frac{r}{2z} + 1} \cdot dz. \end{aligned} \quad (7)$$

Thus, the distance from a point on the isophase curve H to the corresponding point on the mandrel surface Q is

$$|HQ| = \int_{P \rightarrow Q} \sin \alpha \sqrt{\frac{r}{2z} + 1} \cdot dz. \quad (8)$$

From Fig. 9, the distance AH can be expressed as

$$|AH| = |AQ| - |HQ| = f(z_G^Q, \tan \theta'), \quad (9)$$

which is a function of the Z coordinate of point Q and angle θ' .

From Eq. (5), given a point $Q(y'^Q, z_G^Q)$ on the mandrel surface, we have a corresponding point $A(y'^A, z_G^A)$ on the CGH1 surface. So Eq. (9) can also be expressed as

$$|AH| = g(y'^A, \tan \theta'). \quad (10)$$

To determine the expression of function g , a set of value $\{z_G^Q\}$ and a set of $\{\tan \theta'\}$ are chosen. From Eqs. (4) and (5), we can calculate the sets $\{y'^A\}$ and $\{z_G^A\}$. Then from Eqs. (6) and (8), the values of $|AQ|$ and $|HQ|$ can be calculated. According to Eq. (9), we then get the set of $\{|AH|\}$. By a 2-D polynomial fitting of set $\{|AH|\}$ to set $\{y'^A\}$, and set $\{\tan \theta'\}$, we obtain an approximation for $|AH|$,

$$|AH| = \sum_i \sum_j \omega_{i,j} \cdot (\tan \theta')^i \cdot (y'^A)^j. \quad (11)$$

According to Figs. 8 and 9 and Eq. (3), we have

$$y'^A = \sqrt{(x_G^A)^2 + (y_G^A)^2}, \quad \text{and } \tan \theta' = \frac{y_G^A \cdot \tan \theta}{\sqrt{(x_G^A)^2 + (y_G^A)^2}}. \quad (12)$$

Then from Eqs. (2), (11), and (12), we finally arrive at the phase function of CGH1:

$$\Phi_1(x,y) = -\Phi_{AH} - \Phi_{\text{tilt}} = \left\{ -\sum_{i=0}^m \sum_{j=0}^n \omega_{i,j} [(y \cos \theta_1 + y_{\text{CGH1}}) \tan \theta_1]^i \cdot \{ [x^2 + (y \cos \theta_1 + y_{\text{CGH1}})^2]^{1/2} \}^{j-i} - y \sin \theta_1 \right\} \cdot \left(\frac{2\pi}{\lambda} \right). \quad (13)$$

$$\mathbf{W} = \begin{pmatrix} 29.6452162 \text{ mm} & 0.31264679 & 1.1567000 \text{ mm}^{-1} & -8.5313883e-12 \text{ mm}^{-2} \\ 0.0016655 \text{ mm} & -0.9498954 & 2.0929989 \text{ mm}^{-1} & -2.3299297 \text{ mm}^{-2} \\ 0.2760099 \text{ mm} & -0.0042953 & 2.1995551e-5 \text{ mm}^{-1} & -3.7017251e-8 \text{ mm}^{-2} \\ 11.2454690 \text{ mm} & -0.1748034 & 0.0008936 \text{ mm}^{-1} & -1.5030973e-6 \text{ mm}^{-2} \end{pmatrix}.$$

This is the sought-after expression. The second term in Eq. (13) is a tilt component. In Eq. (13), the maximum order of i and j is typically not very high, in general third order is adequate for negligible wavefront error. This greatly reduces the ripple seen from the tenth-order expressions required for a standard x - y polynomial in the CGH plane for a comparable rms error.

The methodology employed for solving the phase function for CGH2 is similar, except there is no tilt phase component because rays will be diffracted and propagate back along the incident direction (Littrow geometry assumed.) Under this assumed geometry, the semianalytical expression of the phase function of CGH2 equals:

$$\mathbf{W} = \begin{pmatrix} 11.9137322 \text{ mm} & 0.3185599 & 1.0000855 \text{ mm}^{-1} & 1.5727386e-11 \text{ mm}^{-2} \\ 0.00216867 \text{ mm} & -0.9479249 & 1.3214069e-7 \text{ mm}^{-1} & -1.4634755e-10 \text{ mm}^{-2} \\ -0.0003151 \text{ mm} & -0.0000140 & 1.2286619e-7 \text{ mm}^{-1} & 4.8776761e-10 \text{ mm}^{-2} \\ 0.0003203 \text{ mm} & -0.0000990 & 1.0622771e-6 \text{ mm}^{-1} & 4.1167531e-9 \text{ mm}^{-2} \end{pmatrix}.$$

5 Fiducials and Tolerances

Fiducials are used to establish the cavity geometry. They serve as guides to eliminate all the degrees of freedom of movement between the two CGHs and are an essential element of the method. We plan to also make some fiducials on the mandrel to aid stitching, but this is not discussed here.

5.1 Design of the Alignment Fiducials

There are four types of fiducials encoded into our CGHs in addition to the main pattern (see Fig. 10): fine alignment

where (x, y) is the local coordinate of a point on the CGH1 surface, in units of millimeters. For the demonstration setup, we chose $m=n=3$ and wavelength $\lambda=0.6328 \times 10^{-3}$ mm. Then the values of $\omega_{i,j}$ are, in matrix form,

$$\Phi_2(x,y) = 2 \cdot \left(-\sum_{i=0}^m \sum_{j=0}^n \omega_{i,j} (y \cos \theta_2 + y_{\text{CGH2}}) \tan \theta_2 \right)^i \times \left\{ \sqrt{[x^2 + (y \cos \theta_2 + y_{\text{CGH2}})^2]^{1/2}} \right\}^{j-i} \cdot \frac{2\pi}{\lambda}, \quad (14)$$

where (x, y) is the local coordinate of a point on the CGH2 surface, in units of millimeters. For the demonstration setup, with $m=n=3$,

fiducials for CGH1 to CGH2; rough alignment fiducials for CGH1 to CGH2; alignment fiducials for CGH1 to the interferometer; and alignment fiducials for CGH1 to the mandrel. In this section, we discuss the alignment fiducials for CGH1 to CGH2, which establish the cavity and are a unique feature of the CGH cavity metrology technique.

The rough alignment fiducials are three small zone plates, distributed at about 120 deg around the main pattern area of CGH1 [see Fig. 10(a)], which focus the collimated beam to three etched points on the CGH2 surface [see Fig. 10(b)], which places CGH2 near its ideal position.

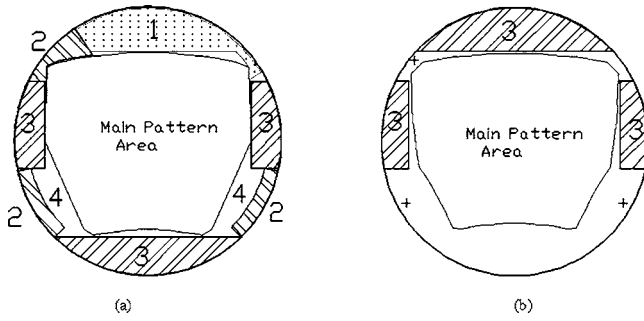


Fig. 10 Layout of fiducials on (a) CGH1 and (b) CGH2. Area 1: fiducial of CGH1 to interferometer; area 2: rough alignment fiducials of CGH1 to CGH2; area 3: fine alignment fiducials of CGH1 to CGH2; and area 4: fiducials of CGH1 to mandrel. The three cross marks on CGH2 are for rough alignment of CGH2 to CGH1.

There are also two sets of fine alignment fiducials on CGH1, which focus the collimated beam from the interferometer into two line foci along the x and y axes, respectively between CGH1 and CGH2. After being diffracted by the fiducial patterns on CGH2, a confocal system is formed. These fiducials have a fast effective aperture (about $f/1.33$), which reduces the z tolerance of the cavity. The chosen phase functions assure a high sensitivity to centering error, distance error, and errors in rotation about the x , y , and z axes of CGH2 relative to the CGH1 surface.

The phase functions we chose for these fiducials on CGH1 are

$$\varphi_x(x,y) = -\{[x^2 + (y \sin \theta_1 - z_{\text{focal}})^2]^{1/2} - z_{\text{focal}} + y \sin \theta_1\} \cdot \frac{2\pi}{\lambda}, \quad (15)$$

$$\varphi_y(x,y) = -\{[(y \cos \theta_1)^2 + (y \sin \theta_1 - z_{\text{focal}})^2]^{1/2} - z_{\text{focal}} + y \sin \theta_1\} \cdot \frac{2\pi}{\lambda}. \quad (16)$$

The phase functions for the fiducials on CGH2 are

$$\varphi_x(x,y) = -2\{[x^2 + [y \sin \theta_2 - (d - z_{\text{focal}})]^2]^{1/2} - (d - z_{\text{focal}})\} \cdot \frac{2\pi}{\lambda}, \quad (17)$$

$$\varphi_y(x,y) = -2\{(y \cos \theta_2)^2 + [y \sin \theta_2 - (d - z_{\text{focal}})]^2\}^{1/2} - (d - z_{\text{focal}})\} \cdot \frac{2\pi}{\lambda}, \quad (18)$$

where θ_1 and θ_2 are the tilt angle of CGH1 and CGH2, z_{focal} is the z coordinate of the confocal image, and d is the distance between CGH1 and CGH2. The layout of the fine alignment fiducial systems in Eqs. (15) and (17) are shown in Fig. 11. Based on an assumed 1/40 wave peak-to-valley interferometric detection limit of the fine alignment fiducials of CGH1-CGH2, the CGH-cavity uncertainty of the demonstration setup is shown in Table 1. This table indicates a performance better than the metrology goal for the demonstration. Table 1 assumes no writing errors and dif-

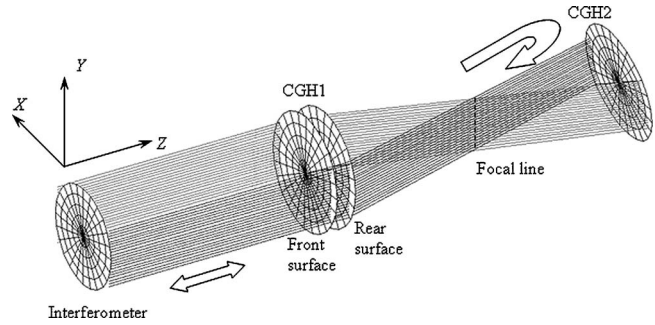


Fig. 11 Fine alignment fiducial system expressed by Eq. (15) and (17). The beams passing through the fine alignment fiducials on CGH1 are focused into a common line focus. A confocal system is formed by the wavefront transmitted by CGH1, reflected by CGH2, and transmitted again by CGH1 back to the interferometer.

fraction effects as well as perfect substrates. In practice, our ability to characterize the substrates and subtract their errors will limit what we can achieve.

5.2 Example

In this example, the tested mandrel is a paraboloid section with radius of curvature at the vertex $r=0.3903$ mm. The diameter of the surface is about 250 mm for the section to be tested, and the axial length is 275 mm. The grazing angle is 71.6 deg, CGH1 tilt angle is 1 deg, and CGH2 tilt angle is 10 deg as measured from the interferometer axis. CGH1's substrate is fused silica and CGH2 is assumed Au-coated. Both CGH1 and CGH2 have a diameter of 140 mm on substrates of 150 mm in diameter. As stated before, the axial distance between CGH1 and CGH2 is 400 mm.

In this case, the minimum feature sizes of CGH1 and CGH2 are 1 and 0.88 μm , respectively. The OSLO optical design software (Lambda Research Corporation, Littleton, Massachusetts) was employed to perform the tolerance calculations. Figure 12(a) shows the residual wavefront error resulting from truncating the polynomial expansion at the third order in Eqs. (12) and (13). Figure 12(b) illustrates the wavefront error for a mandrel with a 1" pure slope error. A pure slope error is defined here as only a change in slope without an error in average radius. This requires an axial

Table 1 Cavity geometric uncertainties for the demonstration setup based on an assumed 1/40 wave P-V interferometric detection limit.

Term (relative position of CGH2 to CGH1)	Uncertainty
Δx	0.01 μm
Δy	0.01 μm
Δz	0.025 μm
$\Delta \chi$ (\odot around x axis)	0.01"
$\Delta \psi$ (\odot around y axis)	0.006"
$\Delta \varphi$ (\odot around z axis)	0.0015"

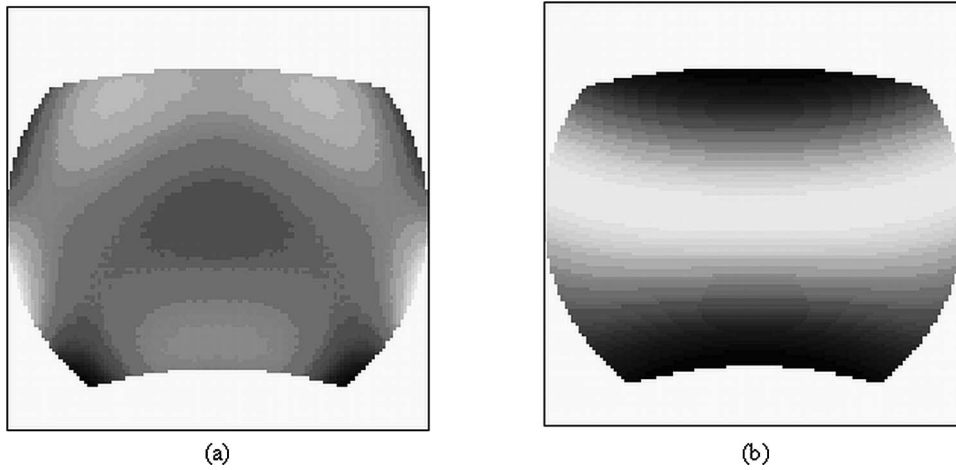


Fig. 12 (a) Simulated interferogram for the residual wavefront error resulting from truncating Eqs. (13) and (14) to third order, the P-V value equals 6.498×10^{-5} wavelength, and the rms equals 8.328×10^{-6} wavelength (scale is 1.0×10^{-5} wavelength per fringe). (b) Simulated interferogram that results when testing a mandrel with a 1'' slope error, the P-V value equals 0.1558 wavelength, and the rms value equals 0.02696 wavelength (scale is 1 wavelength per fringe). The wavelength is 0.6328 μm .

displacement and change in radius in Eq. (4). It is seen that this error, which is at the mission requirement, is easily measured even in this proof-of-concept configuration. The tilt fringes in Fig. 12(b) come about because the cavity geometry is independent of the part position and thus cannot be completely cancelled by misaligning the mandrel. It is the well-characterized cavity geometry (see Table 1) that allows us to measure the slope of Fig. 12(b).

6 Conclusions

We generalize the CGH testing method introduced by Dresel et al.,⁸ Kulawic,⁹ and Mantel, Lindlein, and Schwider¹⁰ to the idea of *CGH cavity metrology*. This idea can be applied to a wide range of metrological problems where it is desirable to test both the geometry and surface figure. This comes at the expense of a reduced throughput for the test, so phase CGHs are normally required. (The exception to this rule is the case of the newer polarization-based interferometers, where the ratio of the irradiances of the reference beam and sample beam can be adjusted.) We demonstrate that the technique for the case of a mandrel to be used for slumping the IXO mirrors exceeds the requirements for the mission. We derive a semianalytical phase function for the main CGH pattern that avoids the higher-frequency oscillations ubiquitous to the x - y polynomial phase functions employed by most optical design programs. This reduction of phase ripple is of great importance for testing of mandrels for x-ray applications, and can improve the speed of pattern generation from the phase function. An example fiducial scheme is outlined that constrains the cavity geometry and thus the test and mandrel geometry. Although this fiducial scheme is only one of many that could be devised, the need for this type of fiducial is unique to CGH cavity metrology. The fiducial scheme's sensitivity will ultimately determine the test geometry sensitivity.

We demonstrate the sensitivity and utility of the CGH cavity method through the example of a mandrel possessing a very small slope error. We find that the slope error shows up both as a wavefront tilt and much smaller magnitude

higher-order wavefront aberration terms. Without the cavity geometry being established independently of the mandrel under test, only the very small higher-order terms would be seen, greatly reducing the test's sensitivity and introducing degeneracies in the possible geometries that could produce them. The elimination of this ambiguity is the chief advantage of CGH cavity metrology over conventional CGH testing (or refractive null testing), and allows both the wavefront and geometry to be determined simultaneously.

Acknowledgments

The authors would like to thank the Innovative Partnership Program at NASA Goddard Space Flight Center for supporting a portion of this work, and Quandou Wang, Jiyoung Chu, and Richard Kasica at NIST, and Alexander Poleshchuk (Institute of Automation and Electrometry, Novosibirsk, Russia) for fruitful discussions.

Appendix

In this appendix, we derive the relation between the coordinates of a point Q on the mandrel surface and the corresponding point A on the CGH1 surface.

Referring to Fig. 9, we denote the directional vector of ray AQ as (l, m) . The normal vector of the mandrel surface at point Q is $(1/ry'^Q, -1)$, where r is the radius of curvature at the vertex of the mandrel. Because the ray is incident on the mandrel surface at angle α , we have,

$$\frac{1}{r} \cdot (-y'^Q \cdot l - m) = \cos \alpha. \quad (19)$$

$$\left\{ (l^2 + m^2) \cdot \left[\left(\frac{1}{r} \cdot (-y'^Q) \right)^2 + 1 \right] \right\}^{1/2} = \cos \alpha.$$

From Eq. (19), we have,

$$\frac{m}{l} = \frac{-V + \sqrt{V^2 - 4UW}}{2U}, \quad (20)$$

where

$$U = \left[\frac{(y'^Q)^2}{r^2} + 1 \right] \cos^2 \alpha - 1, \quad V = 2(y'^Q)/r, \quad \text{and}$$

$$W = U + 1 - \frac{(y'^Q)^2}{r^2}.$$

So the equation of ray AQ can be expressed as,

$$Z - z_G^Q = \frac{m}{l} \cdot (Y' - y'^Q) \quad (21)$$

From Fig. 8, the coordinates of point B are $(0, z_{CGH} - y_{CGH} \tan \theta)$. We can express the line AB in Fig. 9 as,

$$Z = z_{CGH} - y_{CGH} \tan \theta + Y' \tan \theta', \quad (22)$$

where θ' is the angle between line AB and the Y' axis.

Because point A is the intersection of line AB and ray AQ , by solving Eqs. (21) and (22), we obtain the coordinates of point A ,

$$\begin{cases} y'^A = \frac{z_{CGH} - y_{CGH} \tan \theta - z_G^Q + m/l \cdot y'^Q}{m/l - \tan \theta'} \\ z_G^A = z_{CGH} - y_{CGH} \tan \theta + y'^A \tan \theta' \end{cases} \quad (23)$$

If we set $T = m/l$, from Eqs. (20) and (23), we have

$$\begin{cases} y'^A = \frac{z_{CGH} - y_{CGH} \tan \theta - z_G^Q + Ty'^Q}{T - \tan \theta'} \\ z_G^A = z_{CGH} - y_{CGH} \tan \theta + y'^A \tan \theta' \end{cases}, \quad (24)$$

where

$$T = \frac{-V + \sqrt{V^2 - 4UW}}{2U}, \quad U = \left(\frac{(y'^Q)^2}{r^2} + 1 \right) \cos^2 \alpha - 1$$

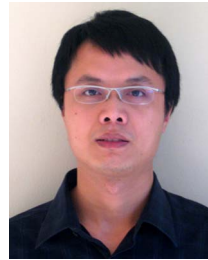
$$V = 2(y'^Q)/r, \quad \text{and} \quad W = U + 1 - \frac{(y'^Q)^2}{r^2}.$$

This is Eq. (5).

References

1. T. T. Saha and W. W. Zhang, "Equal-curvature grazing incidence x-ray telescopes," *Appl. Opt.* **42**, 4599–4605 (2003).
2. R. Petre, J. P. Lehan, S. O'Dell, S. Owens, P. B. Reid, T. Saha, J. Stewart, W. D. Jones, and W. W. Zhang, "The Constellation-X spectroscopy x-ray telescope: recent technology development," *Proc. SPIE* **6266**, 62661Q (2006).
3. D. Vernani, S. Basso, M. Bello, O. Citterio, G. Grisoni, G. Pareschi, D. Spiga, G. Tagliaferri, and G. Valsecchi, "Feasibility study for the manufacturing of the multilayer X-ray optics for Symbol-X," *Memoir Soc. Astron. Italy* **79**, 283–285 (2008).
4. R. Petre, W. W. Zhang, A. D. Content, T. T. Saha, J. Stewart, J. H. Hair, D. Nguyen, W. A. Podgorski, W. R. J. Davis, M. D. Freeman, L. M. Cohen, M. L. Schattenburg, R. K. Heilmann, Y. S. Yanxia, and C. R. Forest, "Constellation-X spectroscopy x-ray telescope (SXT)," *Proc. SPIE* **4851**, 433–440 (2003).
5. S. C. Fawcett, "Diamond turning in the production of x-ray optics," *28th Aerospace Mechan. Symp.*, pp. 91–105 (1994).
6. H. Li, X. Li, and M. W. Grindel, "Measurement of x-ray telescope

- mirrors using a vertical scanning long trace profiler," *Opt. Eng.* **35**(2), 330–338 (1996).
7. W. W. Zhang, D. A. Content, J. P. Lehan, R. Petre, T. T. Saha, M. Gubarev, W. D. Jones, and S. L. O'Dell, "Development of lightweight x-ray mirrors for the Constellation-X mission," *Proc. SPIE* **5900**, 247–257 (2005).
8. T. Dresel, J. Schwider, A. Wehrhahn, and S. Babin, "Grazing incidence interferometry applied to the measurement of cylindrical surfaces," *Opt. Eng.* **34**(12), 3531–3535 (1995).
9. A. W. Kulawiec, "Interferometric measurement of absolute dimensions of cylindrical surfaces at grazing incidence," U.S. Patent 5,777,738 (1998).
10. K. Mantel, N. Lindlein, and J. Schwider, "Simultaneous characterization of the quality and orientation of cylindrical lens surfaces," *Appl. Opt.* **44**, 2970–2977 (2005).
11. K. G. Birch, "Oblique incidence interferometry applied to non-optical surfaces," *J. Phys. E* **6**, 1045–1048 (1973).
12. P. Hariharan, "Improved oblique-incidence interferometer," *Opt. Eng.* **14**(3), 257–258 (1975).
13. I. J. Wilson, "Double-pass oblique-incidence interferometer for the inspection of nonoptical surfaces," *Appl. Opt.* **22**, 1144–1148 (1983).
14. J. Bookbinder, R. Smith, A. Hornschemeier et al., "The Constellation-X Observatory," *Proc. SPIE* **7011**, 7011–02 (2008).
15. J. H. Burge and J. C. Wyant, "Use of computer generated holograms for testing aspheric surfaces," *ASPE Meeting Free-Form Optics*, Chapel Hill, North Carolina, Feb. 4–5 (2004).
16. W. J. Smith, "Optical materials and optical interference coating," Chap. 7 in *Modern Optical Engineering*, 3rd ed., pp. 173–216, McGraw-Hill, New York (2000).



Guangjun Gao received his BE in engineering in 2000 and his PhD in 2005 from Beijing Institute of Technology. He worked as a postdoc at National Astronomical Observatories of China (NAOC), Chinese Academy of Science, from 2005 to 2007. Now he is a guest researcher with the National Institute of Standards and Technology. His research interests include optical design, optical metrology, and diffractive optics.



John P. Lehan received his Bachelor's degree in physics from Virginia Tech, and his Masters and PhD in optical sciences from the University of Arizona. He worked as an industrial researcher prior to coming to NASA Goddard in 2002, working on the Astro-E2 program. In 2004 he began working on the International X-ray Observatory in the role of metrology lead. His research interests include precision optical metrological methods, precision optical measurements, optical testing, optical design, precision optical manufacturing, and scatter from coated and uncoated surfaces.



William W. Zhang is an astrophysicist at the NASA Goddard Space Flight Center. He received his BS degree from Beijing University, where he majored in theoretical physics, and his PhD in experimental particle physics from the University of Pennsylvania. His current research interests include timing studies of neutron stars and black holes. In recent years he has been leading an effort to develop lightweight and high resolution x-ray optics for next-generation observatories. He is developing a high-fidelity replication process by thermally forming thin commercially available glass sheets.



Ulf Griesmann is a physicist with the National Institute of Standards and Technology. He received his Dr.rer.nat degree from the University in Bonn, Germany, in 1992. He worked as a postdoc on atomic spectroscopy with short-wavelength lasers at Imperial College London, United Kingdom. After coming to NIST in 1994, he worked on precision spectrometry and properties of optical materials. His current research interests include optical phase measuring inter-

ferometry, precision form metrology, methods for absolute metrology, and metrology of free-form surfaces.



Johannes A. Soons leads the manufacturing process metrology group at the National Institute of Standards and Technology. He holds a PhD from the Eindhoven University of Technology in the Netherlands. His professional interests include precision machining and optical testing.